Supporting Information

Regulation of Ligand-Induced Solvation Structure for Stable Aqueous Zn-Ion Batteries

Experimental section

Materials

$ZnSO_4 \cdot 7H_2O$ (99.99%), $Zn(CF_3SO_3)_2$ (AR), and V_2O_5 were purchased from Aladdin. 1,3-benzenedimethanol (BDM, 98%), 2,6-pyridinedimethanol (PDM, 97%) and 2,6-pyridinedimethanamine (PDMA, 98%) were purchased from Energy. Zn foils (100 μm) were provided by WengHou Metal Co., Ltd.

Methods

Electrolyte preparation

The electrolytes were prepared by stirring corresponding ligand additives (BDM, PDM and PDMA) in water overnight to obtain homogeneous and transparent solutions, and then the corresponding amount of $ZnSO_4 \cdot 7H_2O$ (2 M) was added into the obtained solution. The optimization concentration for PDM additive was 10 mM. The preparation process of 1 M $Zn(CF_3SO_3)_2$ + 10 mM PDM electrolyte was similar to that of $ZnSO_4$ electrolytes except for adding different Zn salts. The blank control electrolyte was prepared without the addition of ligand additive.

Cathode preparation

V_2O_5 powder, carbon black and polyvinylidene fluoride (PVDF) binder were grinded carefully at a weight ratio of 7:2:1. The electrodes were obtained by blending the mixture in N-methyl-2-pyrrolidone (NMP) and coated the slurry on carbon paper and vacuum dried at 90 ℃ for 12 h. The total mass loading of electrodes was around 3.5 mg cm^{-2}.

Materials Characterization

Contact angles were measured by DataPhysics OCA30 from DataPhysics Instruments Gmb. Fourier-transform infrared spectroscopy (FT-IR) of different electrolytes was done with Bruker Tenser II. The ^1H NMR spectrum was recorded with a 400 Bruker Avance III spectrometer and the data was processed using topspin software package. X-ray diffraction (Xrd) structures of

samples were achieved from Bruker D8 ADVANCE diffractometer with Cu-Kα radiation (λ = 1.5406 Å). The morphology of cycled Zn anodes, deposited Zn and cathodes were observed by scanning electron microscopes (SEM, SHIMADZU) and atomic force microscopes (AFM, BrukerIcon). The surface compositions of Zn anodes with different depths were investigated by X-ray photoelectron spectroscopy (XPS, Thermo fisher Nexsa) through Ar^+ sputtering.

Electrochemical Characterization

The Zn//Zn symmetrical cells, Zn//Cu asymmetric cells and Zn//V_2O_5 full cells were assembled using Zn foil, different counter electrodes, GF/D glass fiber separators and 100 μl corresponding electrolytes in CR2032 coin cells. The basic cells cycling were performed with Land battery testing station (LAND CT2001A) in a constant temperature room. The DoD test was completed using home-made pre-deposition 6 mAh cm^{-2} Zn in Cu substrate electrodes. The chronoamperometry (CA) curves of Zn//Zn were obtained at -150 mV using CHI760e electrochemical workstation. Tafel plots were measured between −0.2 V and +0.2 V of OCV at 1 mV s^{-1} with Zn plate as the working electrode and counter electrode, and Ag/AgCl as the reference electrode, respectively. The hydrogen evolution reaction potential was recorded using linear sweep voltammetry method in 0.5 M Na_2SO_4 electrolyte at 1 mV s^{-1} using Zn plate as the working electrode, Pt plate counter electrode, and Ag/AgCl as the reference electrode. The nucleation overpotential was measured using cyclic voltammetry method at 1 mV s^{-1} between -1.2 V and 0.4 V vs. Ag/AgCl. Electrochemical impedance spectroscopy tests were conducted under a 5 mV amplitude in a frequency range of 0.01 Hz to 10^6 Hz at OCV. The Zn^{2+} transference numbers of different electrolytes were obtained using Bruce-Vincent method with the following equation S1:

$$t_+ = \frac{I_{ss}(\Delta V - I_0 R_0)}{I_0(\Delta V - I_{ss} R_{ss})} \quad \text{(S1)}$$

I_0 and I_{ss} were the current before and after the polarization process. R_0 and R_{ss} were the interfacial resistance before and after polarization process.

Computational methods

Adsorption energy calculations: The calculation related to the interaction between Zn crystal and molecules were performed by DMol3 code in Material Studio software, with Perdew-Burke-Ernzerhof (PBE) generalized gradient approximation (GGA) and double-numerical properties plus polarization (DNP) functions as base set in the convergence tolerance, the energy, force, and displacement were set as 10-6 Ha, 0.004 Ha/Å, and 0.005 Å, separately. To avoid the influence of periodic adjacent layers, a vacuum layer of 15 Å was used in the direction of vertical substrate plane. The absorbed energy between Zn slab and different molecules was defined as following equation S2:

$$E_{adsorb} = E_{Zn-slab+molecules} + E_{Zn-slab} - E_{molecules} \quad \text{(S2)}$$

Molecular dynamics (MD) simulations: Two amorphous cells were constructed: (1) 5555 H_2O, 200 $ZnSO_4$, and (2) 5555 H_2O, 200 $ZnSO_4$, 1 PDM. The intial size of amorphous cell is 9 × 9 × 9 nm^3. In the simulation, the geometry optimization procedure with energy convergence tolerance of 2 × 10^{-5} kcal mol^{-1} was first performed to obtain low potential energy characteristics using Smart Minimized method. Afterward, the cell was subjected to 1 ns of NVT ensemble and 2 ns of NPT to maintain constant density and obtain the most stable configuration. The 3D periodic boundary condition was applied. The pressure and temperature were controlled by Andersen barostat and Berendsen thermostat, respectively. The Verlet velocity time integration method with a time step of 1 fs was used to integrate the Newtonian equation of motion. The van der Waals interactions were calculated by the Lennard-Jones function with a cutoff distance of 12.5 Å and the electrostatic interactions were approximated by the Ewald method with an accuracy of 0.001 kcal/mol. All modeling and simulation were performed Material Studio software with COMPASS force field.

Density Functional Theory (DFT) calculations: The DFT calculations were executed using DMol3 code in the framework of the general gradient approximation (GGA) within the Perdew-Burke-Ernzerhof (PBE) exchange correlation functional. The double numerical plus

polarization (DNP) was utilized as the numerical basis set during the simulation. The core electrons treatment was implemented by DFT semicore pseudopotential. The Monkhorst-Pack grid of 2×2×1 k-point was used. A Fermi smearing of 0.005 Ha and a global orbital cutoff of 3.7 Å were set. The geometric optimizations were performed with a self-consistent field convergence tolerance of 10^{-6} Ha/atom, energy convergence tolerance of 10^{-5} Ha, maximum force convergence tolerance of 0.002 Ha/Å, and maximum displacement convergence tolerance of 0.005 Å. The Electrostatic potential (ESP) were analyzed according to the optimized results. The binding energies (E_B) were calculated using DMol3 code by the following equation S3:

$$E_B = E_{com} - \sum E_{fra} \quad \text{(S3)}$$

where E_{com} is the total energy of the complex, E_{fra} is the energy of each fragment.

Supporting Figures and tables

Fig. S1. Optical photo of 2 M $ZnSO_4$ electrolytes with 10 mM BDM, 10 mM PDM and 10 mM PDMA after preparation for 6 months.

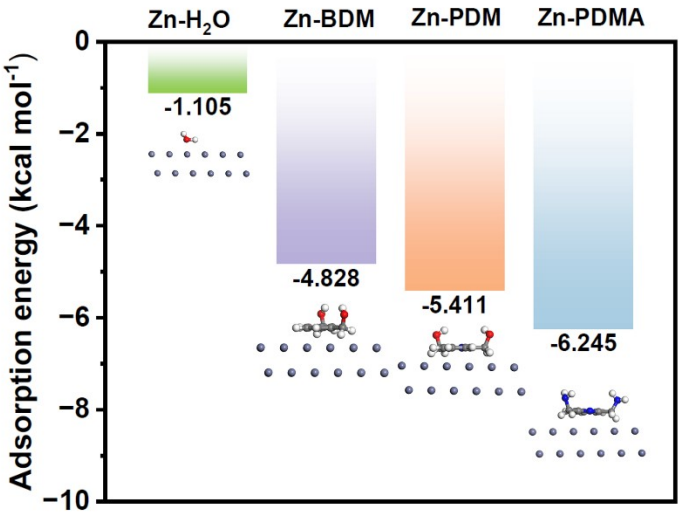

Fig. S2. Absorption energy comparison of H_2O and three ligand additives on Zn (002) crystal plane, insets show the corresponding absorbed models for different situations.

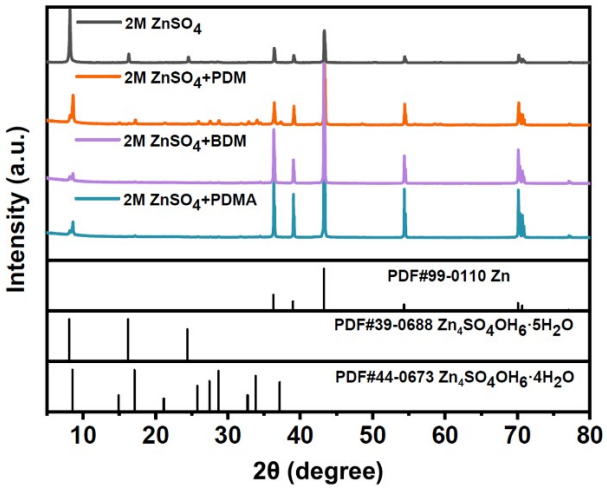

Fig. S3. XRD patterns of Zn anodes after 20 cycles at 1 mA cm^{-2}, 1 mA h cm^{-2} in different electrolytes.

As shown in **Fig. S3**, the peaks of $Zn_4SO_4(OH)_6 \cdot 4H_2O$ can only be observed in curves with additives, especially that of PDM. This may be explained by that more SO_4^{2-} are brought by the PDM additive at the electrode-electrolyte interface.

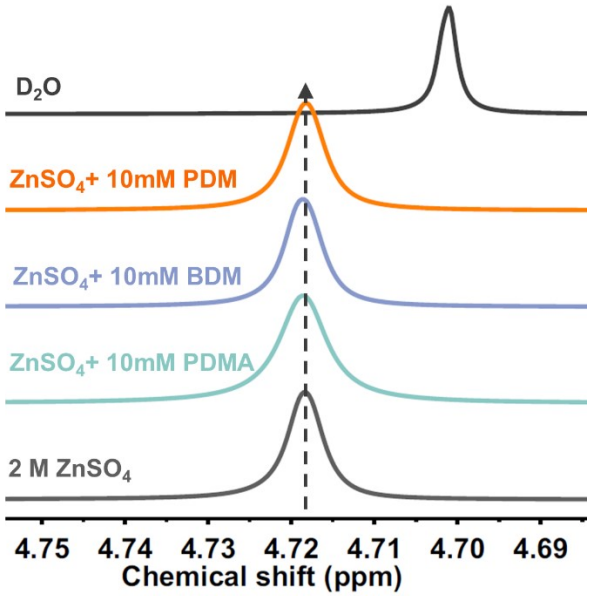

Fig. S4. ^1H NMR spectra of H_2O, 2 M $ZnSO_4$, 2 M $ZnSO_4$ with 10 mM PDM, 2 M $ZnSO_4$ with 10 mM BDM and 2 M $ZnSO_4$ with 10 mM PDMA in D_2O.

As shown in **Fig. S4**, when 10 mM BDM or 10 mM PDMA was included in 2 M $ZnSO_4$, the peak shift to the opposite field slightly compared with PDM, implying their different effects on the regulation of Zn-ion solvation sheaths.

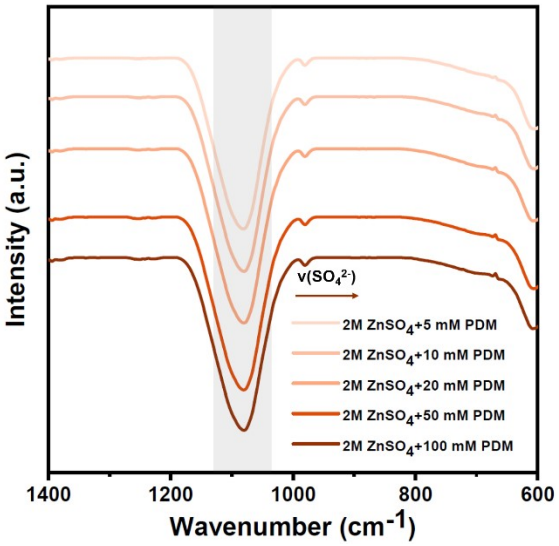

Fig. S5. FT-IR spectra of the electrolytes containing different concentration of PDM.

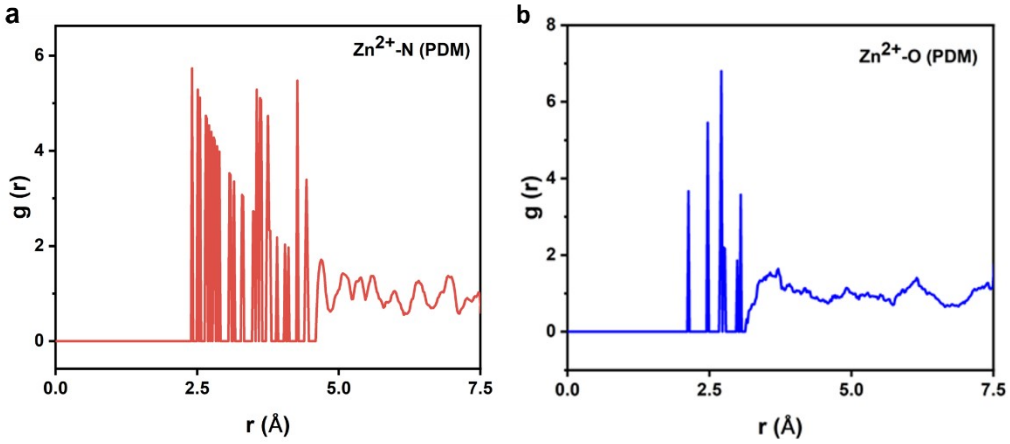

Fig. S6. RDF of (a) Zn^{2+} with N, (b) Zn^{2+} with O of PDM in electrolyte with PDM.

As can be observed in **Fig. S6**, the first peak of Zn^{2+}-N from PDM locates at 2.40 Å , and first peak of Zn^{2+}-O from PDM locates at 2.13 Å, implying PDM ligand can enter the PSS of Zn^{2+}.

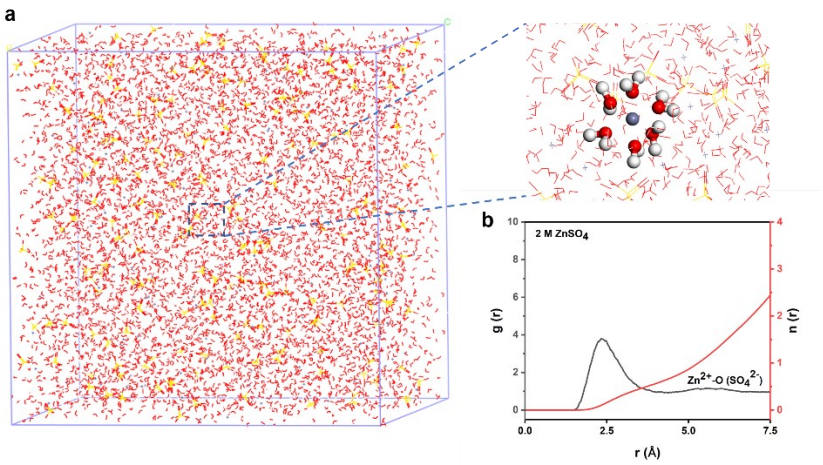

Fig. S7. (a) Snapshot of 2 M $ZnSO_4$ electrolyte system from MD simulation, and partial enlarged snapshot representing Zn^{2+} solvation structure. (b) RDF and coordination number of Zn^{2+}-O (SO_4^{2-}) in 2 M $ZnSO_4$ electrolyte.

As demonstrated in **Fig. S7**, in original 2 M $ZnSO_4$ electrolyte, six water molecules coordinating with Zn^{2+} form PSS. From RDF, we can see that peak of Zn-O from SO_4^{2-} is gentle and the corresponding coordination number is vague, which is in sharp contrast with that in 2 M $ZnSO_4$ + PDM electrolyte. Therefore, we can conclude that with the help of PDM ligand additive, more SO_4^{2-} molecules are brought into Zn-ion PSS.

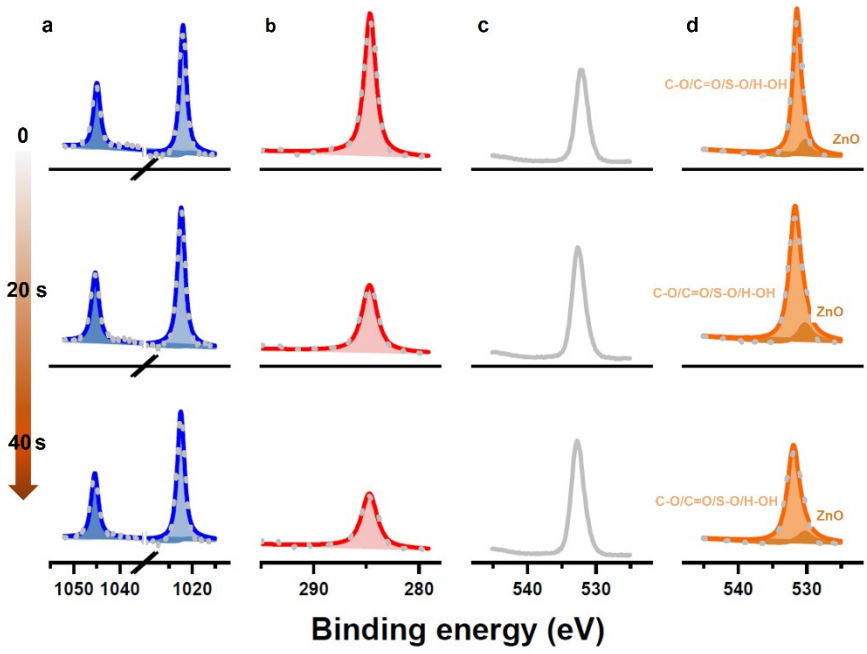

Fig. S8. XPS spectra of Zn anode before and after sputtering. (a) Zn 2p, (b) C 1s, (c) O 1s with pure 2 M $ZnSO_4$. (d) O 1s with 2 M $ZnSO_4$ +PDM electrolytes.

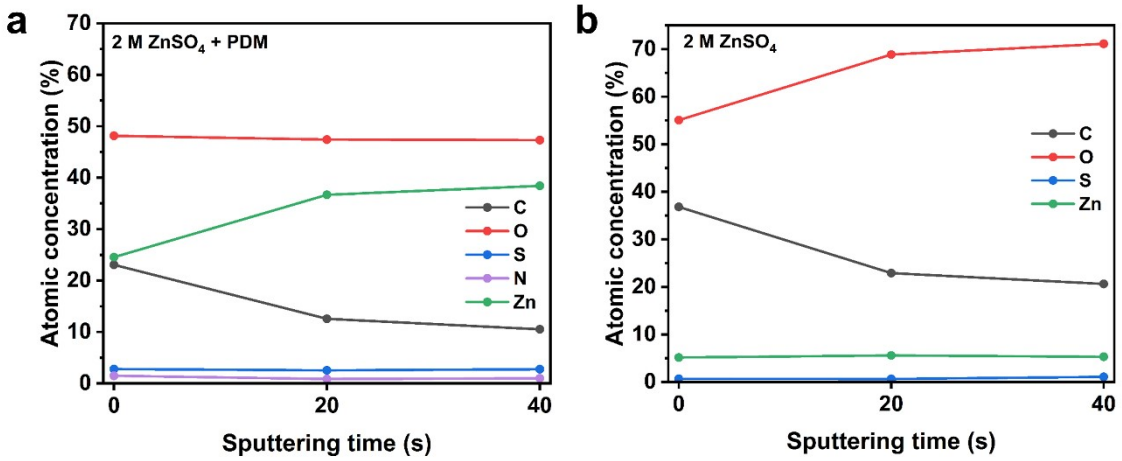

Fig. S9. The calculated elements concentration changes of cycled Zn anode with different sputtering times in (a) 2 M $ZnSO_4$ + PDM, (b) 2 M $ZnSO_4$ electrolyte.

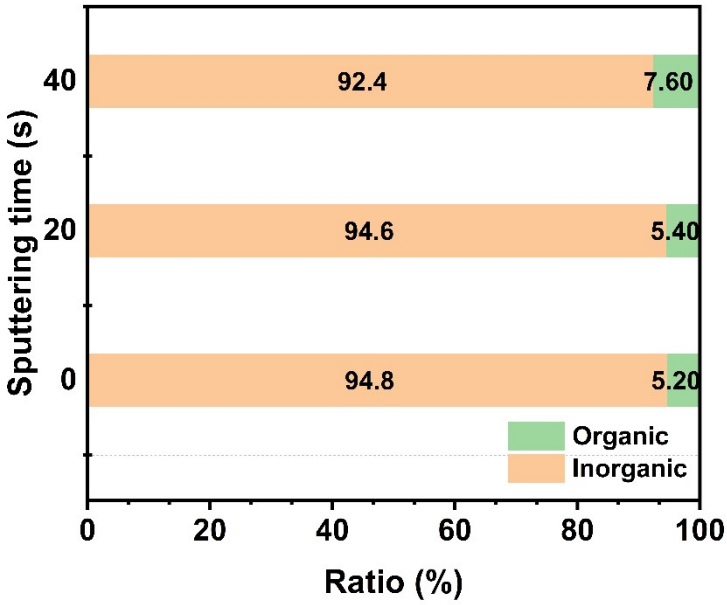

Fig. S10. The calculated components of SEI on cycled Zn anode with different sputtering times in 2 M $ZnSO_4$ + PDM electrolyte.

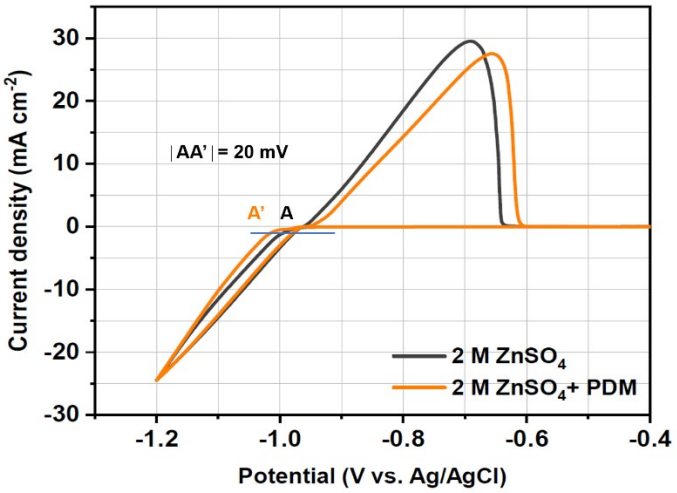

Fig. S11. CV curves of of Zn//Cu in 2 M $ZnSO_4$ and 2 M $ZnSO_4$ + PDM electrolytes.

As demonstrated in **Fig. S11**, the nucleation overpotential (NOP) was evaluated significantly with 20 mV. The critical Zn nucleus radius and NOP follows the equation S4:

$$r_{crit} = 2\frac{\gamma V_m}{F|\eta|} \quad \text{(S4)}$$

γ is surface energy of Zn-electrolyte interface, V_m is molar volume of Zn, F is Faraday's constant, and η is NOP. We can infer that a higher NOP leads to a more fine-grained Zn depositon.[S1,S2] Therefore, the addition of PDM promotes the uniform Zn deposition.

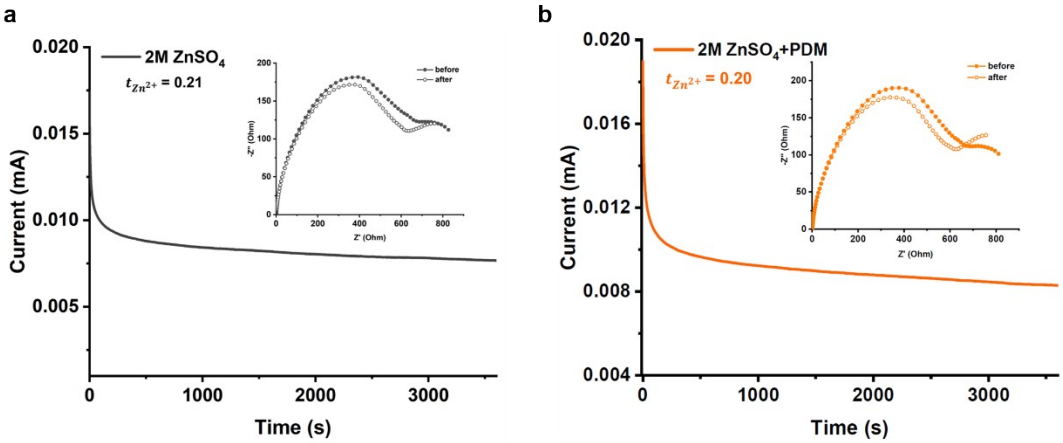

Fig. S12. Transference number of Zn^{2+} in (a) 2 M $ZnSO_4$, and (b) 2 M $ZnSO_4$ + PDM electrolytes.

As shown in **Fig. S12**, the cation transference number in PDM containing electrolyte is almost the same as that in neat $ZnSO_4$ electrolyte, indicating the altered PSS does not retard the transportation of Zn^{2+}.

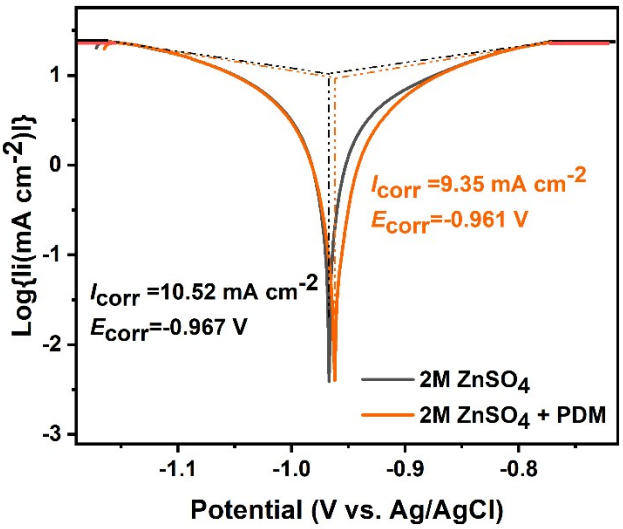

Fig. S13. Tafel curves of of Zn anodes in $ZnSO_4$ and $ZnSO_4$ + PDM electrolytes at a scan rate of 1 mV s^{-1}.

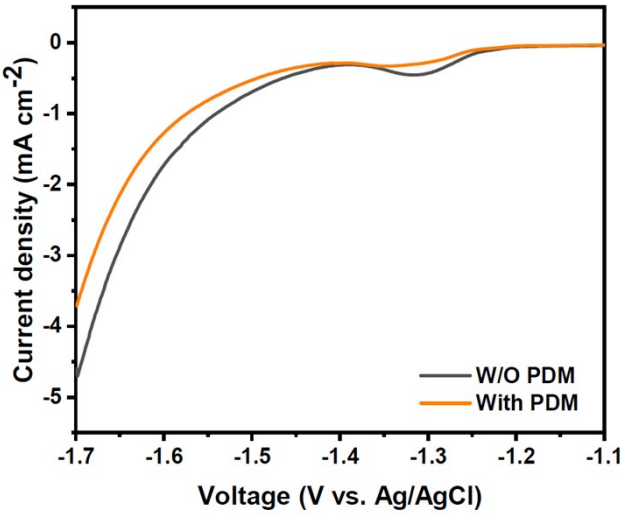

Fig. S14. LSV curves of 2 M $ZnSO_4$ and 2 M $ZnSO_4$ + PDM electrolytes in Na_2SO_4 electrolytes at a scan rate of 1 mV s^{-1}.

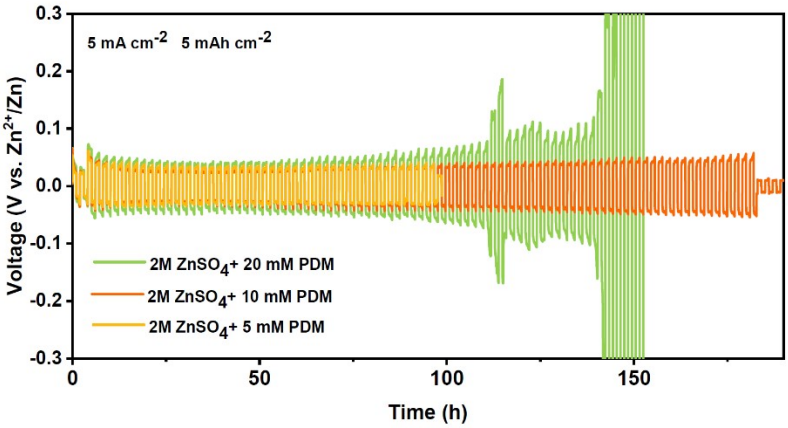

Fig. S15. Voltage profiles of Zn//Zn symmetric cells at 5 mA cm^{-2}, 5 mAh cm^{-2} with electrolytes containing different concentration of PDM.

As shown in **Fig. S15**, less or more than 10 mM PDM leads to a shorter life-span of Zn//Zn symmetric cells, which could be attributed to that 5 mM PDM additives are too little to support the formation and durability of the SEI layer and 20 mM PDM additives result in excessive strong interactions between large amount of PDM additives and Zn^{2+}. Therefore, we adopted 2 M $ZnSO_4$ + 10 mM PDM electrolyte and conducted the following experiments.

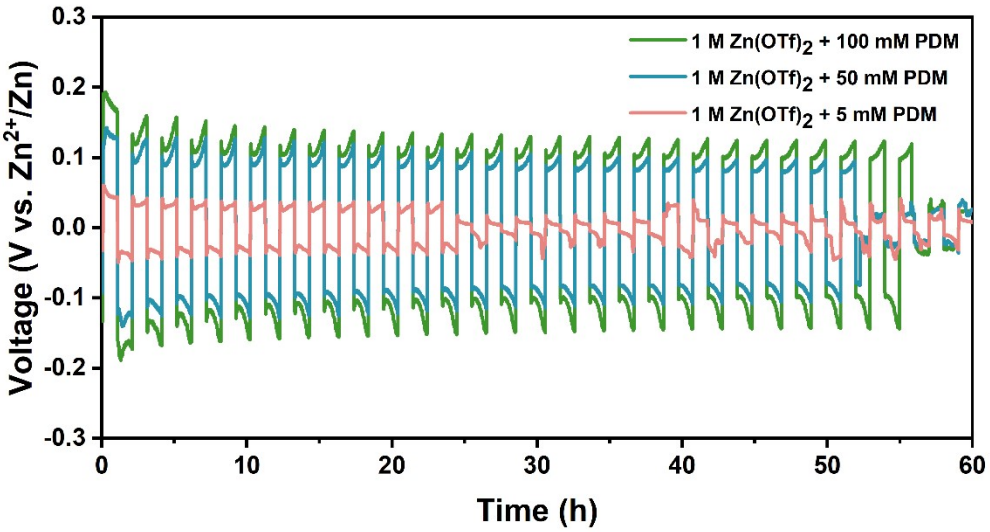

Fig. S16. Voltage profiles of Zn//Zn symmetric cells at 5 mA cm^{-2}, 5 mAh cm^{-2} in electrolytes with 1 M $Zn(OTf)_2$ and different concentrations of PDM.

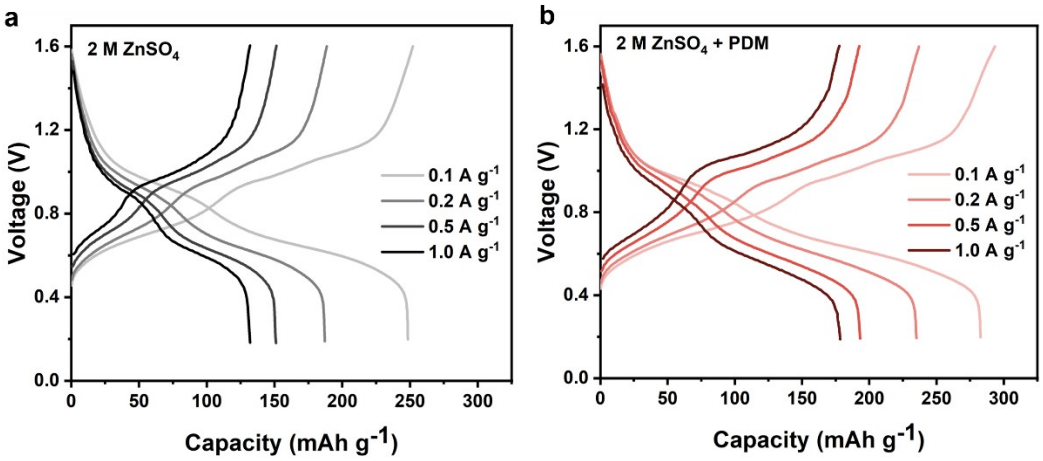

Fig. S17. Voltage-capacity curves of Zn//V_2O_5 cells at differnent current densities in (a) 2 M $ZnSO_4$, (b) 2 M $ZnSO_4$ + 10 mM electrolyte.

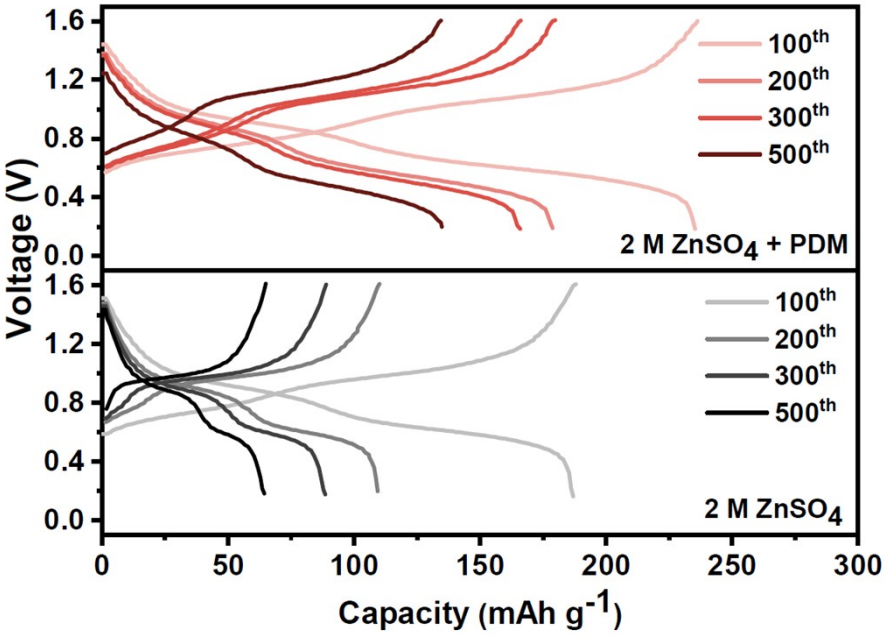

Fig. S18. The galvanostatic charge/discharge curves of Zn//V_2O_5 full cells at specific cycles in different electrolytes (Top: 2 M $ZnSO_4$ + PDM, bottom: 2 M $ZnSO_4$).

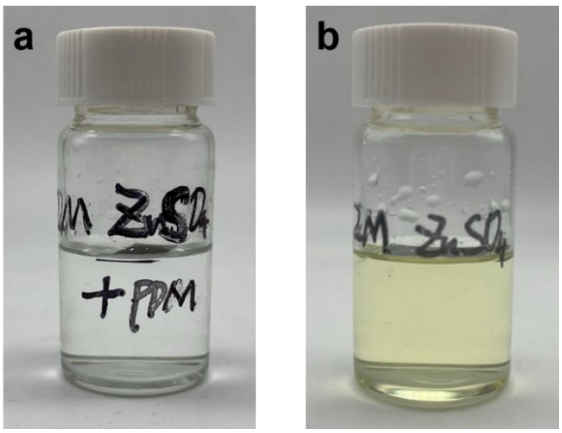

Fig. S19. Optical images of cathode immersed in (a) 2 M $ZnSO_4$ + PDM, (b) 2 M $ZnSO_4$ different electrolytes after 7 days.

Table S1. The DFT calculation results of atomic distances between Zn^{2+} and ligand additives, SO_4^{2-}, respectively.

	d (Å)		d (Å)		d (Å)
PDM (O_1)	2.191	BDM (O1)	2.068	PDMA (N_1)	2.147
PDM (O_2)	2.191	BDM (O2)	4.893	PDMA (N_2)	2.148
PDM (N)	1.998	**SO_4^{2-} (O)**	**2.000**	PDMA (N_3) on the ring	2.063
SO_4^{2-} (O)	**1.931**			**SO_4^{2-}(O)**	**1.979**

From the listed atomic distances in **Table S1**, we can conclude that PDM is closest to Zn^{2+}, and can repel solvated H_2O and provide possibilities for SO_4^{2-} to enter Zn-ion PSS. Since BDM is a monodentate ligand, with only one O atom on one side coordinating with Zn^{2+}, its repulsive force is relatively small compared with PDM. Therefore, BDM cannot make enough room for the entrance of SO_4^{2-}. Although PDMA also is a chelating ligand like PDM, its coordination strength with Zn^{2+} is stronger. The distances between N atoms on the "arms" of PDMA and Zn^{2+} are shorter than those of comparable O atoms of PDM. Therefore, we can infer that Zn^{2+} is surrounded by PDMA more tightly, which stops SO_4^{2-} from entering into the PSS.

References

[S1] Z. Zhao, J. Zhao, Z. Hu, J. Li, J. Li, Y. Zhang, C. Wang, G. Cui, *Energy Environ. Sci.*, 2019, **12**, 1938.

[S2] D. Kashchiev, *J. Chem. Phys.*, 1982, **76**, 5098.